ACS OMEGA

http://pubs.acs.org/journal/acsodf

Article

Effective Atomic N Doping on CeO_2 Nanoparticles by Environmentally Benign Urea Thermolysis and Its Significant Effects on the Scavenging of Reactive Oxygen Radicals

Jihun Paick, Seunghee Hong, Ji-Young Bae, Jy-Young Jyoung, Eun-Sook Lee, and Doohwan Lee*

Cite This: *ACS Omega* 2023, 8, 22646−22655

Read Online

ACCESS | Metrics & More | Article Recommendations

ABSTRACT: Atomic nitrogen doping on CeO_2 nanoparticles (NPs) by an efficient and environmentally benign urea thermolysis approach is first studied, and its effects on the intrinsic scavenging activity of the CeO_2 NPs for reactive oxygen radicals are investigated. The N-doped CeO_2 (N-CeO_2) NPs, characterized by X-ray photoelectron and Raman spectroscopy analyses, showed considerably high levels of N atomic doping (2.3−11.6%), accompanying with an order of magnitude increase of the lattice oxygen vacancies on the CeO_2 crystal surface. The radical scavenging properties of the N-CeO_2 NPs are characterized by applying Fenton's reaction with collective and quantitative kinetic analysis. The results revealed that the significant increase of surface oxygen vacancies is the leading cause for the enhancements of radical scavenging properties by the N doping of CeO_2 NPs. Enriched with abundant surface oxygen vacancies, the N-CeO_2 NPs prepared by urea thermolysis provided about 1.4−2.5 times greater radical scavenging properties than the pristine CeO_2. The collective kinetic analysis revealed that the surface-area-normalized intrinsic radical scavenging activity of the N-CeO_2 NPs is about 6- to 8-fold greater than that of the pristine CeO_2 NPs. The results suggest the high effectiveness of the N doping of CeO_2 by the environmentally benign urea thermolysis approach to enhance the radical scavenging activity of CeO_2 NPs for extensive applications such as that in polymer electrolyte membrane fuel cells.

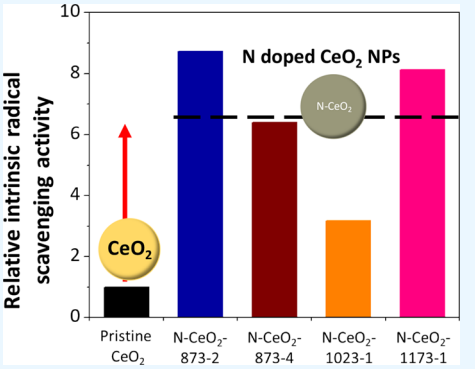

1. INTRODUCTION

In recent years, cerium oxides have attracted much attention for application as a radical scavenger in polymer electrolyte membrane fuel cells (PEMFCs) to mitigate the membrane degradation caused by reactive radical species, such as hydroxyl and hydroperoxyl radicals, generated during the fuel cell operation.[1] These reactive oxygen species (ROS) initiate the oxidative decomposition of the polymer membrane; therefore, the in situ removal of the ROS by regenerative radical scavengers can improve the durability and lifetime of the PEMFCs.[2] Previous studies have reported that an addition of ceria nanoparticles (NPs) in the perfluorosulfonated acid (PFSA) membranes, such as Nafion, and the catalyst layer of the membrane electrode assembly (MEA) led to the significant mitigation of the membrane degradation attributed to radical scavenging by the ceria NPs.[2−9] The radical scavenging properties are reported with various metal oxides, such as ZrO_2, YSZ, TiO_2, MnO_2, and silica-supported Mn, Cr, and Co oxides.[5,9−12] However, cerium oxides and modified cerium oxide materials seem to offer antioxidant properties superior to that of other metal oxides reported in the literature.[13] The regenerative radical scavenging properties of cerium oxides are typically described with the redox cycles between the reduced Ce^{3+} and the oxidized Ce^{4+} states involving the lattice oxygen vacancies on the surface.[14,15]

For the applications in the scavenging of ROS, there have been significant studies to enhance the radical scavenging properties of cerium oxides.[16] It is reported that the size and exposed crystal facets of ceria NPs have considerable effects on the radical scavenging activity because a decrease in particle size leads to an increase in the Ce^{3+}/Ce^{4+} ratio accompanying the formation of oxygen vacancies.[13] Most of the previous studies have focused on the enhancements of the radical scavenging activity of CeO_2 by heterometal doping, such as that with La,[17−19] Eu,[18,20] Nd,[18] Gd,[21] Pr,[18,21] W,[22] and Zr.[21,23−25] The enhancements of the radical scavenging activity by the incorporation of heterometal cations of different valances and sizes in CeO_2 are generally rationalized with an increase in the surface oxygen vacancies or the relative Ce^{3+}

Received: February 26, 2023
Accepted: June 1, 2023
Published: June 14, 2023

© 2023 The Authors. Published by American Chemical Society

concentration and in some cases an increase in the surface area.[21]

The physicochemical properties of metal oxides can also be modified by partial replacements of the lattice oxygen atoms with various nonmetallic heteroatoms of different valence states. For example, atomic nitrogen doping has been applied for the modification of metal oxide properties, such as tuning the band gap of TiO_2[26] and CeO_2[27,28] for photocatalytic applications. An enrichment of oxygen vacancies by N doping of CeO_2 was also reported, which provided enhanced catalytic activities for the selective catalytic reduction of nitrogen oxides for automotive applications.[29] However, only a few studies on the N-doped CeO_2 NPs for free-radical scavenging applications have been reported.[30] Furthermore, the N doping of metal oxides in previous studies was typically conducted by treatments of ceria NPs in a toxic NH_3 gas flow at high temperatures,[27,29,31] surface coating with polyaniline by controlled polymerization, followed by heat treatments,[30] and solvothermal synthesis of N-doped CeO_2 using cerium salts and nitrogen precursors.[28,32] These previous N doping methods require toxic chemicals or extensive processes with limited scalability and cost competitiveness.

Herein, we first report a highly effective approach for the surface N doping of CeO_2 NPs via an environmentally benign urea thermolysis approach. As will be discussed, a controlled thermal treatment of a mixture of CeO_2 NPs and urea powder under an inert atmosphere resulted in atomic N doping with significant increases in the Ce^{3+} and oxygen vacancy concentrations on the CeO_2 surface. The resulting N-CeO_2 NPs exhibited considerable enhancements in the scavenging activities for the reactive hydroxyl radicals, as characterized by applying Fenton's reaction. Collective and quantitative kinetic analysis reveals that the enhancements in the radical scavenging activity of the N-CeO_2 NPs are primarily attributed to the increase of surface oxygen vacancies by the N doping treatment. Normalized with the surface area, the N-CeO_2 NPs provided about 6- to 8-fold greater intrinsic radical scavenging activities over the pristine CeO_2, indicating the high effectiveness of the N doping of CeO_2 NPs by urea thermolysis for the radical scavenging applications.

2. EXPERIMENTAL SECTION

2.1. Materials. Pristine CeO_2 powder (Sigma-Aldrich), urea (98%, Alfa Aesar), rhodamine-B (Alfa Aesar), $FeSO_4$ (98.5%, Junsei Chem.), H_2O_2 (30 wt %, DaeJung Chem.), and N_2 gas (99.999%, Deokyang Korea) were purchased and used as received.

2.2. Atomic N Doping of CeO_2 Nanoparticles. The atomic nitrogen doping of CeO_2 NPs was conducted through the thermolysis of urea at elevated temperatures of 873, 1023, and 1173 K. The pristine CeO_2 NPs were mixed with urea powder at various weight ratios (CeO_2/urea = 1.0−4.0) and placed in a ceramic sample boat. The sample boat was covered with a ceramic plate and placed inside a horizontal tubular quartz reactor (I.D. = 50 mm, L = 1200 mm) equipped with a temperature-controlled electric furnace. Both ends of the reactor were capped gas-tight, and an inert N_2 gas flow (100 mL min^{-1}) was introduced into the reactor for purging at 298 K for 1 h. The N atomic doping of the CeO_2 NPs was conducted at three different temperatures of 873, 1023, and 1073 K. The reactor temperature was raised (ramp = 15 K min^{-1}) by flowing N_2 gas through the reactor and held at the N doping temperature for 2 h. Finally, the reactor was cooled to room temperature under the N_2 gas flow. The resulting N-doped CeO_2 NPs are named N-CeO_2-T−W, where T is the doping temperature in Kelvin, and W is the weight ratio of the CeO_2/urea mixture utilized for N doping.

2.3. Characterizations. The thermal decomposition characteristics of urea ($CO(NH_2)_2$) powder were obtained by thermogravimetric analysis (TGA, Pyris-1, PerkinElmer), raising the sample temperature from 298 to 1173 K (ramp = 10 K min^{-1}) under N_2 atmosphere. The surface composition of the pristine CeO_2 and the N-doped CeO_2 samples was characterized by X-ray photoelectron spectroscopy (XPS) with monochromatic Al-Kα radiation (Theta Probe AR-XPS, Thermo Fisher Scientific). The Ce^{3+} and Ce^{4+} atomic contents in the samples were obtained by the deconvolution of the peaks at the Ce 3d binding energy level.[30,33] The atomic content and structural configuration of the N species on the N-CeO_2 NPs were obtained by the deconvolution of the N 1s peak of the XPS spectra. The morphology and surface composition of the pristine CeO_2 and the N-CeO_2 NPs were characterized by scanning electron microscopy (SEM, SNE-3000M, SEC) at an accelerating voltage of 30 kV equipped with an EDS system. The crystal structure of the samples was characterized by X-ray diffraction (XRD, SmartLab, Rigaku), with monochromatic Cu-Kα radiation operated at 3 kW (scan rate = 0.05° min^{-1}). The concentration of surface oxygen vacancies on the samples was characterized by Raman spectroscopy (Vertex 80, Bruker) conducted at 532 nm laser wavelength. The number of oxygen vacancies was calculated from the full width at half-maximum (FWHM) of the characteristic Raman peak, according to the method reported in the literature.[30,34] The N_2 adsorption−desorption isotherms of the samples were obtained in a volumetric unit (Tristar-II, Micromeritics), after drying the samples under vacuum at 423 K for 12 h. The specific surface area of the samples was obtained from the N_2 sorption isotherms, applying the Brunauer−Emmett−Teller (BET) method. The total pore volume of the samples was obtained by single-point N_2 adsorption at the saturation pressure.

2.4. Measurement of the Radical Scavenging Properties. The radical scavenging properties of the pristine CeO_2 and N-CeO_2 NPs were characterized by applying Fenton's reaction in the co-presence of rhodamine-B (RhB) and the radical scavenger in the solution. First, 50 mg of the pristine CeO_2 or N-CeO_2 NPs was added to 2 mL of an aqueous solution containing RhB (0.6 mg), $FeSO_4$ (3 mg), and H_2O (100 mL) under stirring. Second, an aqueous solution of H_2O_2 (0.08 vol %) was prepared using H_2O_2 (30 wt %) and DI water. Then, a fixed amount (3 μL) of H_2O_2 solution was added dropwise to the first solution and stirred for 10 min. The UV−vis spectra of the solution mixture were obtained using a UV−vis spectrometer (Mega-800, Sinco) in the range of 300−700 nm. This procedure was repeated at 10 min intervals for 1 h to measure the change of RhB concentration in the solution with time. The radical scavenging properties of the pristine CeO_2 and the N-CeO_2 NPs were estimated from the decay rate of RhB concentration in the solution, in comparison to the decay rate in the blank Fenton's reagent solution without adding a radical scavenger. The measurement was conducted at least three times for each sample to ensure the reproducibility and reliability of the data.

https://doi.org/10.1021/acsomega.3c01305
ACS Omega 2023, 8, 22646−22655

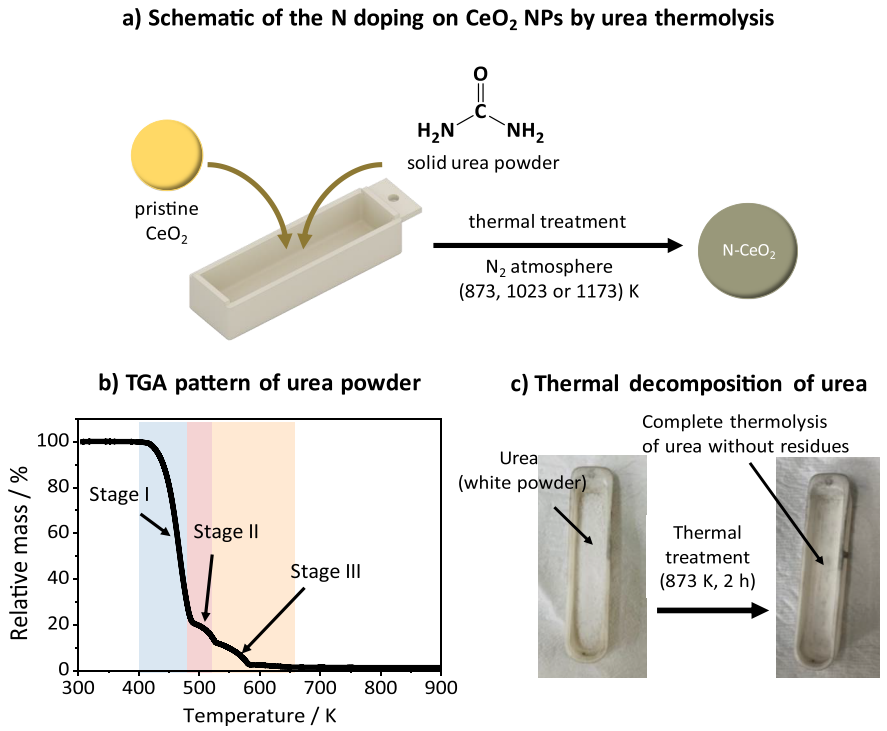

Figure 1. (a) Schematic of N doping on CeO_2 nanoparticles by urea thermolysis, (b) weight loss profile of the solid urea powder by thermolysis characterized by thermogravimetric analysis (TGA) in N_2 atmosphere, (c) photographs of the urea powder taken before and after thermal treatment at 873 K for 2 h in N_2 atmosphere.

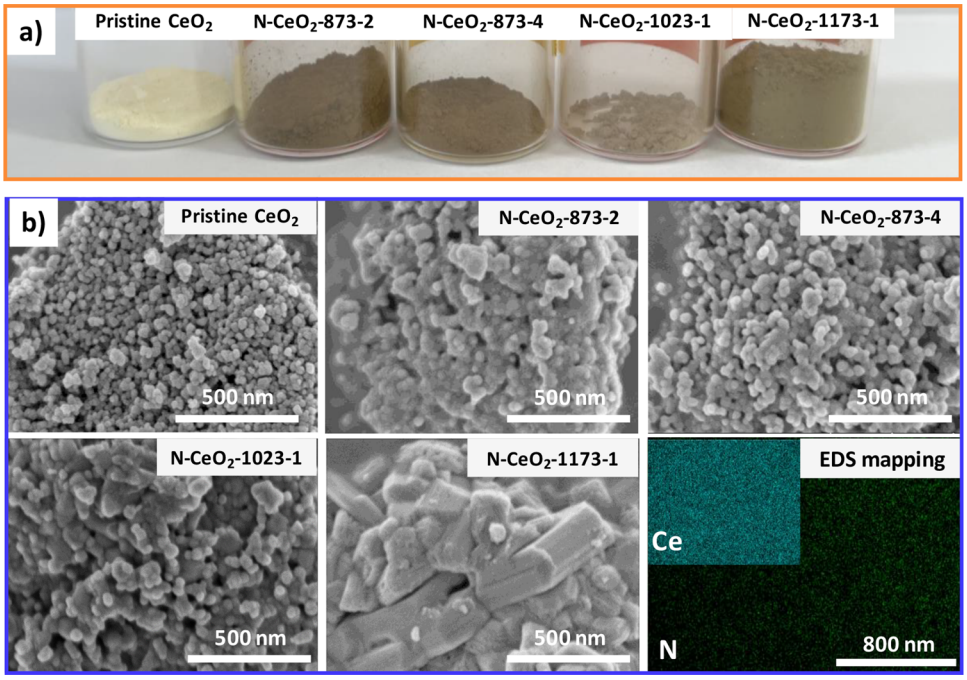

Figure 2. (a) Photographs of the pristine CeO_2 and N-CeO_2 NPs prepared at various CeO_2/urea weight ratios and reaction temperatures, (b) SEM images of the pristine CeO_2 and N-doped CeO_2 samples with the EDS elemental mapping on the N-CeO_2-873-4 sample.

3. RESULTS AND DISCUSSION

3.1. Atomic N Doping of CeO_2 NPs by Urea Thermolysis. Figure 1a describes the N doping of CeO_2 NPs by urea thermolysis studied in this work. Briefly, a simple thermal treatment of CeO_2 NPs as a mixture with urea powder under an inert N_2 atmosphere results in the effective N doping of CeO_2 NPs with high levels of surface N concentration. The method is highly effective, scalable, and environmentally benign without requiring any toxic precursors, reagents, or cumbersome pre- and post-treatment steps. Figure 1b shows the typical TGA profile of urea powder under an inert N_2 atmosphere. The results show that the thermal decomposition of urea occurs through three distinct steps in terms of temperature. The major weight loss (~80 wt %) occurred

https://doi.org/10.1021/acsomega.3c01305
ACS Omega 2023, 8, 22646−22655

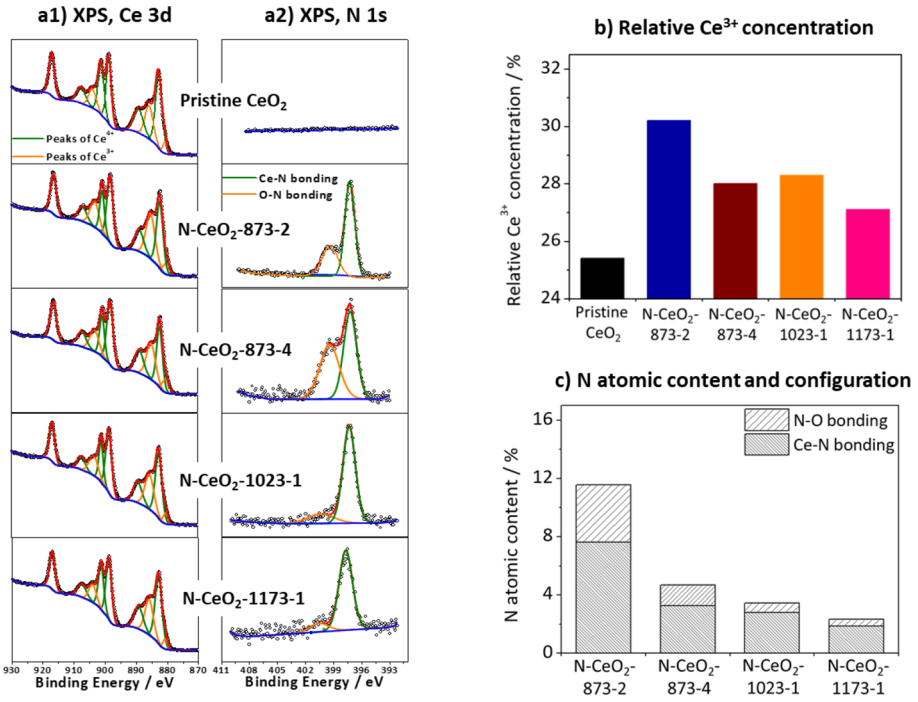

Figure 3. (a) XPS spectra of the pristine CeO_2 and the N-doped CeO_2 NPs at Ce 3d and N 1s binding energy levels, (b) relative Ce^{3+} concentration defined as $Ce^{3+}/(Ce^{3+} + Ce^{4+})$ atomic ratio on the samples, and (c) atomic contents and bonding configuration of the N species on the N-CeO_2 NPs.

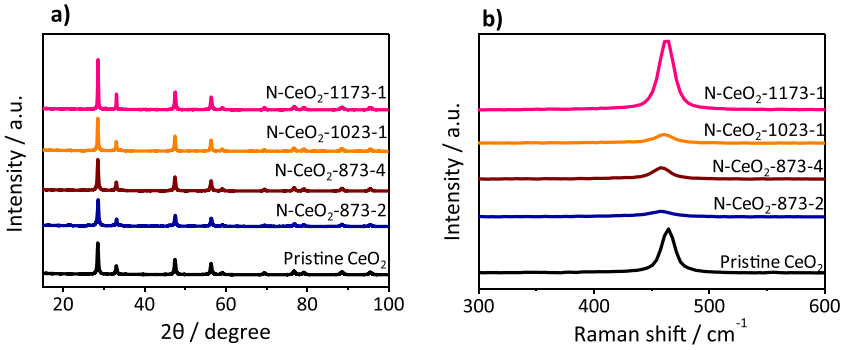

Figure 4. (a) XRD patterns and (b) Raman spectra on the pristine CeO_2 and the N-doped CeO_2 NPs.

between 450 and 480 K, which accounts for the decomposition of urea to NH_3. At this stage, the formation of biuret (NH_2−CO−NH−CO−NH_2) can also take place, which undergoes further complex decomposition and polymerization at higher temperatures.[35,36] The second- and third-stage weight losses at around 560 and 630 K, respectively, can be attributed to the decomposition of the biuret and triuret species to NH_3 and CO_2.[37] Figure 1c shows the photographs of urea powder before and after heat treatment at 873 K for 1 h under an inert N_2 atmosphere. After the heat treatment, the photograph does not show the urea powder (white solids) or any decomposition residues remaining in the sample boat, confirming the complete thermolysis of urea at the given condition.

3.2. Physicochemical Properties of the N-Doped CeO_2 NPs. Figure 2a shows the photograph of the pristine CeO_2 and the N-doped CeO_2 (N-CeO_2) samples prepared by the urea thermolysis of CeO_2/urea mixtures at various weight ratios (2−4) and temperatures (873, 923, and 1073 K). The pristine CeO_2 shows a typical bright yellow color, while the N-CeO_2 samples exhibit various colors depending on the thermal treatment temperature: dark brown (873 K), light brown (1023 K), and greenish gray (1173 K). Figure 2b compares the typical SEM images of the pristine CeO_2 and N-doped CeO_2 samples. The pristine CeO_2 displays round-shaped individual CeO_2 nanoparticles, of size in the approximate range (20−50) nm. The N-CeO_2-873-2 and N-CeO_2-873-4 NPs show nearly identical particle sizes and shapes to those of the pristine CeO_2, suggesting no significant morphological changes or aggregation of CeO_2 NPs by the N doping treatment at 873 K. The EDS elemental mapping results exhibit uniform N concentration over the N-CeO_2-873-4 NPs, reflecting the high effectiveness of the urea thermolysis method for the N doping of CeO_2 NPs.

The SEM images of the N-CeO_2-1173-1 NPs reveal that the particle sizes of the crystallites have increased significantly by the thermal treatment at the excessively high temperature.

Figure 3a shows the deconvoluted XPS spectra for the quantification of the atomic contents and structural configurations of the Ce and N species on the CeO_2 and the N-CeO_2 NPs. Figure 3b displays the relative Ce^{3+} concentration,

https://doi.org/10.1021/acsomega.3c01305
ACS Omega 2023, 8, 22646−22655

Table 1. Cubic Lattice Parameter, BET Surface Area, Pore Volume, and Oxygen Vacancy Concentration of the Pristine CeO_2 and the N-Doped CeO_2 NPs

	XRD	N_2 adsorption		Raman spectroscopy
sample	cubic lattice parameter, a (Å)	surface area ($m^2\ g^{-1}$)	pore volume ($cm^3\ g^{-1}$)	oxygen vacancy concentration ($\times 10^{20}$ vacancies cm^{-3})
pristine CeO_2	5.412	31.8	47.1	0.21
N-CeO_2-873-2	5.403	5.4	10.7	8.66
N-CeO_2-873-4	5.406	12.2	28.7	1.76
N-CeO_2-1023-1	5.409	10.0	12.3	2.00
N-CeO_2-1173-1	5.398	2.4	2.6	0.38

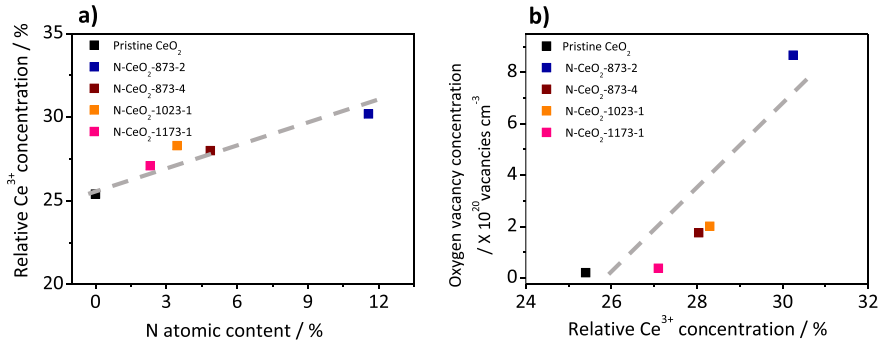

Figure 5. Linear correlation of (a) relative C^{3+} concentration vs surface N atomic content, (b) Surface oxygen vacancy concentration vs the relative C^{3+} concentration on the CeO_2 and N-CeO_2 NPs.

defined by the $Ce^{3+}/(Ce^{4+} + Ce^{3+})$ atomic ratio, on the pristine CeO_2 and the N-CeO_2 NPs obtained by the XPS analysis. Figure 3c shows the surface atomic contents and the structural configurations of the N species doped on the N-CeO_2 samples. The results in Figure 3b reveal that the relative Ce^{3+} atomic concentrations on the N-CeO_2 NPs (27.2−30.1%) are considerably higher than that on the pristine CeO_2 (25.2%). At the same time, the N-CeO_2 samples (Figure 3c) display a high N atomic content on the surface at 2.3−11.6 atomic%. The results show that the N doping amounts on the N-CeO_2 NPs decreased gradually with the increasing thermal treatment temperature. The results also reveal that the N species were doped on CeO_2 dominantly in the configuration of Ce−N covalent bonding (65−81%). In addtion, N−O bonding was observed at a relative concentration of 19−35% of the total surface N species, which is likely attributed to the nitrogen oxides grafted on the surface.

Figure 4a shows the XRD patterns of the pristine CeO_2 and N-CeO_2 NPs. All the samples display the typical diffraction pattern of the cubic FCC crystal structure of CeO_2 (JCPDS #82-0792). No additional diffraction peaks are observed on the N-CeO_2 samples. The N-CeO_2 NPs prepared at high temperatures of 1023 and 1173 K exhibit sharper and more intense XRD peaks, compared to those of the pristine CeO_2 NPs, suggesting an enhancement in their crystallinity by the high temperature doping treatments. The cubic lattice parameter (a, Å) of the pristine CeO_2 and N-CeO_2 NPs is calculated from the (111) diffraction peak of the XRD spectra. Table 1 shows the results. The pristine CeO_2 shows the lattice parameter value of 5.412 Å. The lattice parameter values of the N-CeO_2 samples of 5.398−5.409 Å are slightly smaller than that of the pristine CeO_2, which is likely due to the increased crystallinity of the samples by the treatment at high temperatures. Table 1 also shows the BET surface area and pore volume of the pristine CeO_2 and N-CeO_2 samples. The surface area and pore volume of the N-CeO_2 samples are lower than those of the pristine CeO_2 due to sintering by the high-temperature treatments, in agreement with the XRD results.

The concentration of surface oxygen vacancies on the pristine CeO_2 and N-CeO_2 NPs is estimated by Raman spectroscopy. Figure 4b shows the Raman spectra of the samples. The pristine CeO_2 and the N-CeO_2 NPs exhibit the typical characteristic Raman peak of CeO_2 at 460 cm^{-1}, which is attributed to the symmetrical stretching mode of the Ce−O_8 vibrational unit.[24,38] The concentration of the surface oxygen vacancies on the samples is estimated from the peak broadening.[30,34] Table 1 summarizes the results. The results reveal substantial increases of the oxygen vacancy concentration on the N-CeO_2 NPs, exhibiting about 8−41 times higher oxygen vacancy concentrations on the N-CeO_2 samples prepared at 873 and 1023 K ($(1.76-8.66) \times 10^{20}$ vacancies cm^{-3}), than on the pristine CeO_2 NPs (0.21×10^{20} vacancies cm^{-3}).

3.3. Effects of Atomic N Doping on the Oxygen Vacancy Concentration of CeO_2 NPs. A collective correlation analysis was conducted among the N doping amounts, the relative atomic concentration of Ce^{3+} species, and the surface oxygen vacancy concentration on the pristine CeO_2 and the N-CeO_2 NPs. Figure 5a shows the relative Ce^{3+} concentration, defined as $Ce^{3+}/(Ce^{3+} + Ce^{4+})$ atomic ratio, of the samples as a function of the N doping amounts. The results exhibit a linear correlation between the relative Ce^{3+} concentration and the surface N atomic content, displaying a proportional increase of the relative Ce^{3+} concentration with an increase of N doping amount on the samples. Figure 5b shows the surface oxygen vacancy concentration as a function of the relative Ce^{3+} concentration on the pristine CeO_2 and the N-CeO_2 NPs. The results also show a linear correlation between the surface oxygen vacancy and the relative Ce^{3+} atomic concentrations, exhibiting substantial increases of the oxygen vacancies with the increasing relative Ce^{3+} concentration. The results indicate that the N doping on the CeO_2 NPs resulted in the increase of the Ce^{3+} concentration as well

https://doi.org/10.1021/acsomega.3c01305
ACS Omega 2023, 8, 22646−22655

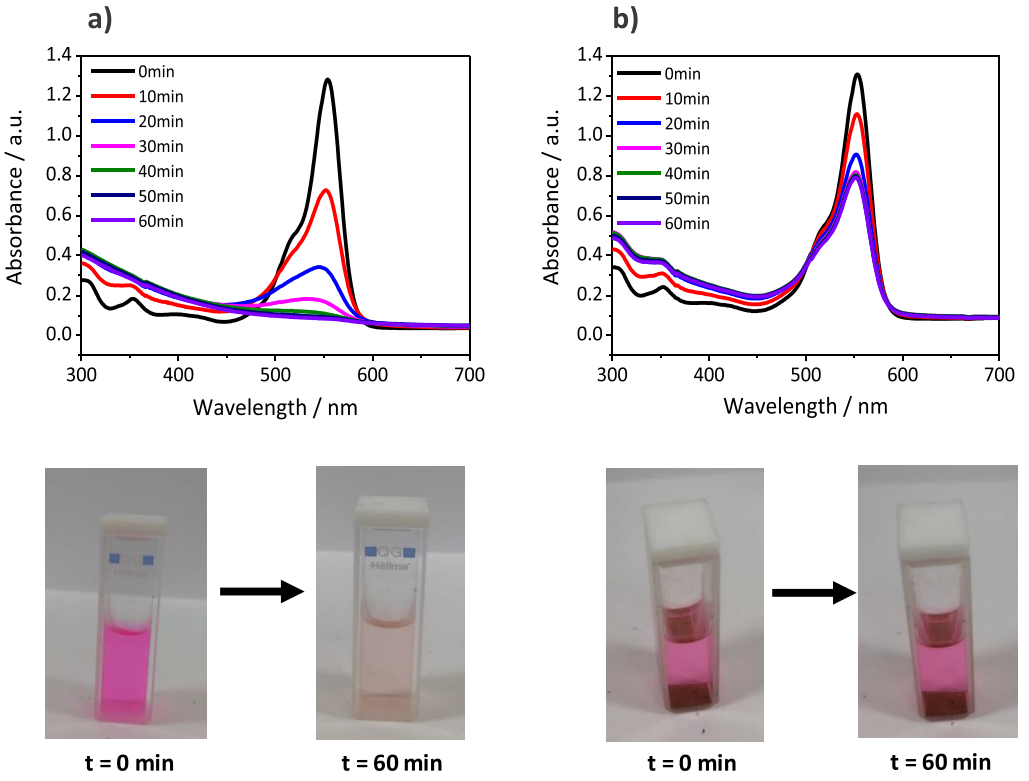

Figure 6. UV−vis spectra of rhodamine-B (RhB) added in (a) blank Fenton's solution and (b) Fenton's solution with N-CeO_2 NPs (25 mg N-CeO_2/mL solution). The photographs of the solution taken before and after the test are shown below the spectra.

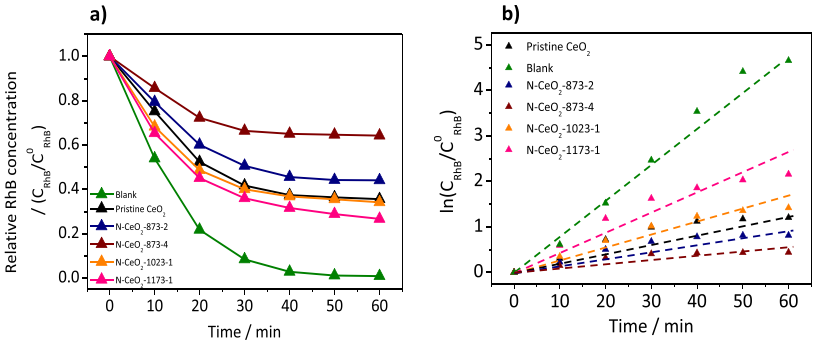

Figure 7. (a) Time-dependent decay of RhB concentration with radical scavengers added in Fenton's solution. (b) Correlation analysis, with the pseudo-first-order degradation kinetics of RhB in the solution.

as the surface oxygen vacancies. The results are reasonable considering that the atomic N doping on CeO_2 NPs would lead to charge imbalance due to the different valency between N and O atoms in the CeO_2 crystal lattice structure.[29] This charge imbalance appears to increase the relative Ce^{3+} concentration and the oxygen vacancies via a charge compensation mechanism.[39]

3.4. Radical Scavenging Properties of the N-Doped CeO_2 NPs. The radical scavenging properties of the pristine CeO_2 and N-CeO_2 NPs are characterized by applying Fenton's reaction in the presence of rhodamine-B (RhB) as a radical scavenging indicator in the solution. Briefly, the hydroxyl radicals generated by Fenton's reactions (eqs 1 and 2) degrade RhB molecules (eq 3); therefore, the relative radical scavenging properties of the materials added to the solution can be estimated from the decay rate of the RhB concentration with time:

$$H_2O_2 + Fe^{2+} \rightarrow HO^{\cdot} + HO^{-} + Fe^{3+} \quad (1)$$

$$Fe^{3+} + H_2O_2 \rightarrow Fe^{2+} + HOO^{\cdot} + H^{+} \quad (2)$$

$$HO^{\cdot} + RhB \rightarrow \text{Degradation of RhB} \quad (3)$$

Figure 6a shows the typical UV−vis spectra of RhB in the Fenton reagent solution taken every 10 min for 1 h, without adding the radical scavengers to the solution (referred to as the blank solution hereafter). The spectra show the peak at 550 nm, which is attributed to the light absorption by RhB molecules in the solution. The results show that the peak intensity attenuates rapidly with time, indicating a significant decrease of RhB concentration due to degradation by the hydroxyl radicals generated by Fenton's reaction. The photographs of the solution taken before and after the test (Figure 6a, bottom) show the large change of solution color, from thick red to light pink, demonstrating the significant

https://doi.org/10.1021/acsomega.3c01305
ACS Omega 2023, 8, 22646−22655

decrease of RhB concentration in the solution. For comparison, Figure 6b shows the UV−vis spectra of the Fenton reagent solution measured in the presence of the pristine CeO_2 NPs (25 mg CeO_2 per 1 mL solution). The results clearly show that the decrease of the peak intensity at 550 nm is much less and slower than that of the blank Fenton solution. The results reflect the substantial radical scavenging effects provided by the pristine CeO_2 NPs added into the solution. The photographs of the solution taken before and after the test (Figure 6b, bottom) clearly display that its initial red color has changed only a little even after the completion of the test, confirming the significant radial scavenging effects provided by the pristine CeO_2 added into the solution.

Figure 7a shows the changes of the relative RhB concentration in the Fenton solution as a function of time after adding the pristine CeO_2 and the N-CeO_2 NPs. The results show that the decrease of RhB concentration is fast and significant in the blank solution. Comparably, the decrease of the RhB concentration is much less in the presence of the pristine CeO_2 NPs, owing to the scavenging of hydroxyl radicals by the CeO_2 NPs added into the solution. Markedly, the N-CeO_2 samples prepared at 873 K exhibit significantly higher radical scavenging properties than the pristine CeO_2, displaying much less and slower decreases of the RhB concentration with time. However, the N-CeO_2 samples prepared at excessive high temperatures (1023 and 1173 K) show radical scavenging properties similar to that of the pristine CeO_2 NPs.

3.5. Quantification of the Radical Scavenging Activity of the N-Doped CeO_2 NPs. For further quantitative analysis, the decomposition kinetics of RhB in Fenton's reagent solution was modeled with a pseudo-first-order reaction rate, assuming that the time-dependent change of the hydroxyl radical concentration in the solution is negligible compared to the RhB concentration (eq 4). This can be justified, as a constant amount of H_2O_2 was repeatedly added into the solution at every 10 min during the test to make its concentration excess, as described in Experimental Section.

$$-r_{RhB} = kC_{HO}.C_{RhB} = k'C_{RhB} \quad (4)$$

Then, the apparent decomposition rate constant, k', can be used to quantify the relative radical scavenging amounts provided by the scavenger materials added into the Fenton reagent solution. An integration of the rate equation with time provides a linear correlation, as shown in eq 4, where C^0_{RhB} is the initial concentration of RhB in the solution, and t is time:

$$-\ln\left(\frac{C_{RhB}}{C^0_{RhB}}\right) = k't \quad (5)$$

The apparent decomposition rate constant of RhB can be obtained by the linear correlation of the experimental results, as shown in Figure 7b. The results clearly show that the pseudo-first-order reaction kinetics of RhB decomposition applied for the analysis is valid. The apparent decomposition rate constant can be obtained from the slopes of the linear data-fitting results, which should be inversely proportional to the radical scavenging activity of the scavenger materials. Table 2 summarizes the apparent decomposition rate constants of RhB obtained by the analysis.

To quantify the relative radical scavenging properties, the apparent decomposition rate constants obtained in the presence of the pristine CeO_2 and N-CeO_2 samples are normalized with the rate constant obtained from the blank Fenton solution. Accordingly, the relative radical scavenging properties are defined as β (eq 6):

$$\beta = \frac{k'(\text{radical scavenger in the solution})}{k'(\text{blank solution})} \quad (6)$$

Table 2. Apparent Decomposition Rate Constants of RhB in the Fenton Solution in the Presence of Pristine CeO_2 and N-CeO_2 Samples

sample	apparent RhB decomposition rate constant, k'
blank	0.0842
pristine CeO_2	0.0344
N-CeO_2-873-2	0.0232
N-CeO_2-873-4	0.014
N-CeO_2-1023-1	0.0344
N-CeO_2-1173-1	0.0561

Figure 8a compares the relative radical scavenging property (β) of the pristine CeO_2 and the N-CeO_2 samples. The results indicate that the pristine CeO_2 NPs provide considerable radical scavenging properties (β = 2.5) at the given conditions, inhibiting the RhB decomposition by scavenging the reactive hydroxyl radicals. The N-CeO_2 NPs prepared at 873 K exhibit high radical scavenging properties, with β values of 3.5−6.2, indicating that their apparent radical scavenging properties are about 140−250% greater than that of the pristine CeO_2 NPs. The N-CeO_2 samples obtained by urea thermolysis at excessive high temperatures (1023 and 1173 K) exhibit similar or slightly smaller β values (2.4−1.5) compared to that of the pristine CeO_2. The results reflect a trade-off of the radical scavenging properties of the N-CeO_2 NPs with the decrease of the surface area by sintering due to the doping treatments at the excessive high temperatures. Figure 8b shows the relative radical scavenging properties (β) of the pristine CeO_2 and N-CeO_2 NPs as a function of the total net amount of oxygen vacancies exposed to the surface of the samples. The total net amount of the surface-exposed oxygen vacancies of a sample can be estimated by multiplying the surface area and the surface oxygen vacancy concentration of each sample. The linear correlation of the β values with the total amount of the surface oxygen vacancies of the pristine CeO_2 and the N-CeO_2 NPs clearly suggests the prominent roles of the oxygen vacancies and surface area in the radical scavenging activity of the samples.

Therefore, it is critical to compare the intrinsic radical scavenging activity of the pristine CeO_2 and the N-CeO_2 NPs, taking into account the different surface areas among the samples. For comparison, the relative intrinsic radical scavenging activity is defined as α (eq 7):

$$\alpha = \frac{\beta(\text{N} - \text{CeO}_2)}{\beta(\text{pristine CeO}_2)} \times \frac{\text{SA(pristine CeO}_2)}{\text{SA(N} - \text{CeO}_2)} \quad (7)$$

where β is the relative radical scavenging property, and SA is the surface area of the sample. Figure 9 shows the relative intrinsic radical scavenging activities of the N-CeO_2 NPs obtained by urea thermolysis in comparison to that of the pristine-CeO_2. The results reveal that the surface-area-normalized intrinsic radical scavenging activity of the N-CeO_2 NPs is more than 6-fold greater, on average, than that of the pristine-CeO_2 NPs.

https://doi.org/10.1021/acsomega.3c01305
ACS Omega 2023, 8, 22646−22655

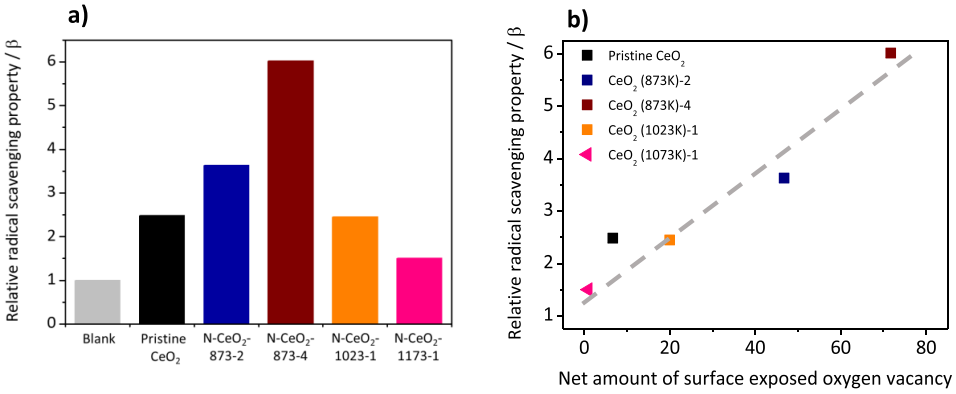

Figure 8. (a) Relative radical scavenging property (β) of the pristine CeO_2 and N-CeO_2 NPs. (b) Correlation of β as a function of the total net amount of surface-exposed oxygen vacancies (surface area × oxygen vacancy concentration of the sample) provided by the samples.

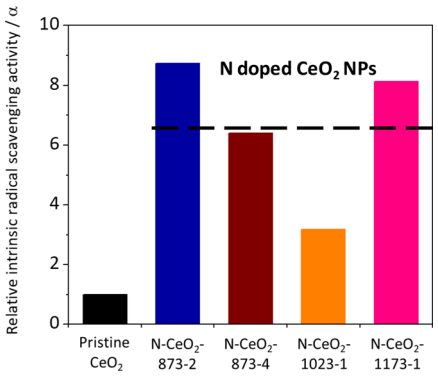

Figure 9. Relative intrinsic radical scavenging activity (α) of the N-CeO_2 NPs obtained by urea thermolysis at 873 K.

Overall, these quantitative analysis results reveal some important findings regarding the effects of N doping on CeO_2 NPs by urea thermolysis for scavenging of reactive oxygen radicals. First, the N doping on CeO_2 NPs leads to a significant increase of the surface oxygen vacancies relevant to the regenerative active sites for the scavenging of hydroxyl radicals. Second, urea thermolysis attempted first in this work is a highly effective, scalable, and environmentally benign approach for the atomic N doping of CeO_2 NPs at high levels of the surface N and oxygen vacancy concentrations.

4. CONCLUSIONS

Highly effective atomic N doping of CeO_2 NPs by a simple and environmentally benign urea thermolysis approach is first studied. A collective and quantitative kinetic analysis was conducted on the effects of N doping of CeO_2 NPs on the scavenging of reactive oxygen radicals in Fenton's reagent solution. The studies reveal that high levels of atomic N doping (2.3−11.6 atomic %) on the surface of CeO_2 NPs can be achieved with covalent Ce−N bonding, resulting in a significant increase of the relative Ce^{3+} contents and oxygen vacancy concentrations. The N-doped CeO_2 NPs provided (1.4−2.5)-fold enhanced radical scavenging properties compared to the pristine CeO_2, where the enhancements depend on the total number of surface oxygen vacancies determined by the surface area and the oxygen vacancy concentration of the samples. Markedly, the collective kinetic analysis suggests that the N-CeO_2 NPs provide more than 6-fold greater surface-area-normalized intrinsic radical scavenging activity than the pristine CeO_2. The results suggest that urea thermolysis is a highly effective method for atomic N doping on CeO_2 nanoparticles for the scavenging of reactive oxygen radicals.

AUTHOR INFORMATION

Corresponding Author

Doohwan Lee − *Department of Chemical Engineering, The University of Seoul, Seoul 02504, Republic of Korea;* orcid.org/0000-0003-2016-8890; Email: dolee@uos.ac.kr

Authors

Jihun Paick − *Department of Chemical Engineering, The University of Seoul, Seoul 02504, Republic of Korea*

Seunghee Hong − *Department of Chemical Engineering, The University of Seoul, Seoul 02504, Republic of Korea*

Ji-Young Bae − *JNTG Co., Ltd., Hwaseong-si, Gyeonggi-do 18523, Republic of Korea*

Jy-Young Jyoung − *JNTG Co., Ltd., Hwaseong-si, Gyeonggi-do 18523, Republic of Korea*

Eun-Sook Lee − *JNTG Co., Ltd., Hwaseong-si, Gyeonggi-do 18523, Republic of Korea*

Complete contact information is available at: https://pubs.acs.org/10.1021/acsomega.3c01305

Notes

The authors declare no competing financial interest.

ACKNOWLEDGMENTS

E.-S.L. acknowledges the financial support from the Institute for Advancement of Technology, which is supported by the Ministry of Trade, Industry, and Energy of the Republic of Korea (grant #P0017349). D.L. acknowledges the support provided by the Basic Study and Interdisciplinary R&D Foundation Fund of the University of Seoul in 2020.

REFERENCES

(1) Rui, Z.; Liu, J. Understanding of free radical scavengers used in highly durable proton exchange membranes. *Prog. Nat. Sci.: Mater. Int.* **2020**, *30*, 732−742.

(2) Prabhakaran, V.; Arges, C. G.; Ramani, V. Investigation of polymer electrolyte membrane chemical degradation and degradation mitigation using *in-situ* fluorescence spectroscopy. *Proc. Natl. Acad. Sci. U. S. A.* **2012**, *109*, 1029−1034.

(3) Wang, L.; Advani, S. G.; Prasad, A. K. Degradation reduction of polymer electrolyte membranes using CeO_2 as a free-radical scavenger in catalyst layer. *Electrochim. Acta* **2013**, *109*, 775−780.

https://doi.org/10.1021/acsomega.3c01305
ACS Omega 2023, 8, 22646−22655

(4) Pearman, B. P.; Mohajeri, N.; Slattery, D. K.; Hampton, M. D.; Seal, S.; Cullen, D. A. The chemical behavior and degradation mitigation effect of cerium oxide nanoparticles in perfluorosulfonic acid polymer electrolyte membranes. *Polym. Degrad. Stab.* **2013**, *98*, 1766−1772.
(5) Weissbach, T.; Peckham, T. J.; Holdcroft, S. CeO_2, ZrO_2 and YSZ as mitigating additives against degradation of proton exchange membranes by free radicals. *J. Membr. Sci.* **2016**, *498*, 94−104.
(6) Pearman, B. P.; Mohajeri, N. M.; Brooker, R. P.; Rodgers, M. P.; Slattery, D. K.; Hampton, M. D.; Cullen, M. D.; Seal, S. The degradation mitigation effect of cerium oxide in polymer electrolyte membranes in extended fuel cell durability tests. *J. Power Sources* **2013**, *225*, 75−83.
(7) Breitwieser, M.; Klose, C.; Hartmann, A.; Buchler, A.; Klingele, M.; Vierrath, S.; Zengerle, R.; Thiele, S. Cerium Oxide Decorated Polymer Nanofibers as Effective Membrane Reinforcement for Durable High-Performance Fuel Cells. *Adv. Energy Mater.* **2017**, *7*, No. 1602100.
(8) Zhiyan, R.; Qingbing, L.; Youxiu, H.; Rui, D.; Jia, L.; Jia, L.; Jianguo, L. Ceria nanorods as highly stable free radical scavengers for highly durable proton exchange membranes. *RSC Adv.* **2021**, *11*, 32012−32021.
(9) Gubler, L.; Koppenol, W. H. Kinetic Simulation of the Chemical Stabilization Mechanism in Fuel Cell Membranes Using Cerium and Manganese Redox Couples. *J. Electrochem. Soc.* **2012**, *159*, B211−B218.
(10) Taghizadeh, M. T.; Vatanparast, M. Ultrasonic-assisted synthesis of ZrO_2 nanoparticles and their application to improve the chemical stability of Nafion membrane in proton exchange membrane (PEM) fuel cells. *J. Colloid Interface Sci.* **2016**, *483*, 1−10.
(11) D'Urso, C.; Oldani, C.; Baglio, V.; Merlo, L.; Aricò, A. S. Immobilized transition metal-based radical scavengers and their effect on durability of Aquivion® perfluorosulfonic acid membranes. *J. Power Sources* **2016**, *301*, 317−325.
(12) Hiroki, A.; LaVerne, J. A. Decomposition of Hydrogen Peroxide at Water−Ceramic Oxide Interfaces. *J. Phys. Chem. B* **2005**, *109*, 3364−3370.
(13) Kwon, H. J.; Shin, K.; Soh, M.; Chang, H.; Kim, J.; Lee, J.; Ko, G.; Kim, B. H.; Kim, D.; Hyeon, T. Large-Scale Synthesis and Medical Applications of Uniform-Sized Metal Oxide Nanoparticles. *Adv. Mater.* **2018**, *30*, No. e1704290.
(14) Lawler, R.; Cho, J.; Ham, H. C.; Ju, H.; Lee, S. W.; Kim, J. Y.; Choi, J. I.; Jang, S. S. CeO_2(111) Surface with Oxygen Vacancy for Radical Scavenging: A Density Functional Theory Approach. *J. Phys. Chem. C* **2020**, *124*, 20950−20959.
(15) Bedar, A.; Singh, B. G.; Tewari, P. K.; Bindal, R. C.; Kar, S. Kinetics studies on free radical scavenging property of ceria in polysulfone−ceria radiation resistant mixed-matrix membrane. *Int. J. Chem. React. Eng.* **2021**, *19*, 779−785.
(16) Montini, T.; Melchionna, M.; Monai, M.; Fornasiero, P. Fundamentals and Catalytic Applications of CeO_2-Based Materials. *Chem. Rev.* **2016**, *116*, 5987−6041.
(17) Fernandez-Garcia, S.; Jiang, L.; Tinoco, M.; Hungria, A. B.; Han, J.; Blanco, G.; Calvino, J. J.; Chen, X. Enhanced Hydroxyl Radical Scavenging Activity by Doping Lanthanum in Ceria Nanocubes. *J. Phys. Chem. C* **2016**, *120*, 1891−1901.
(18) Vinothkumar, G.; Rengaraj, S.; Arunkumar, P.; Cha, S. W.; Babu, K. S. Ionic Radii and Concentration Dependency of RE^{3+} (Eu^{3+}, Nd^{3+}, Pr^{3+}, and La^{3+})-Doped Cerium Oxide Nanoparticles for Enhanced Multienzyme-Mimetic and Hydroxyl Radical Scavenging Activity. *J. Phys. Chem. C* **2019**, *123*, 541−553.
(19) Loche, D.; Morgan, L. M.; Casu, A.; Mountjoy, G.; O'Regan, C.; Corrias, A.; Falqui, A. Determining the maximum lanthanum incorporation in the fluorite structure of La-doped ceria nanocubes for enhanced redox ability. *RSC Adv.* **2019**, *9*, 6745−6751.
(20) Hernández-Castillo, Y.; García-Hernández, M.; López-Marure, A.; Luna-Domínguez, J. H.; López-Camacho, P. Y.; Morales-Ramírez, A. d. J. Antioxidant activity of cerium oxide as a function of europium doped content. *Ceram. Int.* **2019**, *45*, 2303−2308.
(21) Baker, A. M.; Stewart, S. M.; Ramaiyan, K. P.; Banham, D.; Ye, S.; Garzon, F.; Mukundan, R.; Borup, R. L. Doped Ceria Nanoparticles with Reduced Solubility and Improved Peroxide Decomposition Activity for PEM Fuel Cells. *J. Electrochem. Soc.* **2021**, *168*, No. 024507.
(22) Li, Z.; Yang, W.; Xie, L.; Li, Y.; Liu, Y.; Sun, Y.; Bu, Y.; Mi, X.; Zhan, S.; Hu, W. Prominent role of oxygen vacancy for superoxide radical and hydroxyl radical formation to promote electro-Fenton like reaction by W-doped CeO_2 composites. *Appl. Surf. Sci.* **2021**, *549*, No. 149262.
(23) Soh, M.; Kang, D.-W.; Jeong, H.-G.; Kim, D.; Kim, D. Y.; Yang, W.; Song, C.; Baik, S.; Choi, I.-Y.; Ki, S.-K.; Kwon, H. J.; Kim, T.; Kim, C. K.; Lee, S.-H.; Hyeon, T. Ceria−Zirconia Nanoparticles as an Enhanced Multi-Antioxidant for Sepsis Treatment. *Angew. Chem., Int. Ed.* **2017**, *56*, 11399−11403.
(24) Trogadas, P.; Parrondo, J.; Ramani, V. CeO_2 Surface Oxygen Vacancy Concentration Governs in Situ Free Radical Scavenging Efficacy in Polymer Electrolytes. *ACS Appl. Mater. Interfaces* **2012**, *4*, 5098−5102.
(25) Baker, A. M.; Williams, S. T. D.; Mukundan, R.; Spernjak, D.; Advani, S. G.; Prasad, A. K.; Borup, R. L. Zr-doped ceria additives for enhanced PEM fuel cell durability and radical scavenger stability. *J. Mater. Chem. A* **2017**, *5*, 15073−15079.
(26) Asahi, R.; Morikawa, T.; Ohwaki, T.; Aoki, K.; Taga, Y. Visible-Light Photocatalysis in Nitrogen-Doped Titanium Oxides. *Science* **2001**, *293*, 269−271.
(27) Jorge, A. B.; Sakatani, Y.; Boissière, C.; Laberty-Roberts, C.; Sauthier, G.; Fraxedas, J.; Sanchez, C.; Fuertes, A. Nanocrystalline N-doped ceria porous thin films as efficient visible-active photocatalysts. *J. Mater. Chem.* **2012**, *22*, 3220−3226.
(28) Sun, D.; Gu, M.; Li, R.; Yin, S.; Song, X.; Zhao, B.; Li, C.; Li, J.; Feng, Z.; Sato, T. Effects of nitrogen content in monocrystalline nano-CeO_2 on the degradation of dye in indoor lighting. *Appl. Surf. Sci.* **2013**, *280*, 693−697.
(29) Cong, Q.; Chen, L.; Wang, X.; Ma, H.; Zhao, J.; Li, S.; Hou, Y.; Li, W. Promotional effect of nitrogen-doping on a ceria unary oxide catalyst with rich oxygen vacancies for selective catalytic reduction of NO with NH_3. *Chem. Eng. J.* **2020**, *379*, No. 122302.
(30) Prabhakaran, V.; Ramani, V. Structurally-Tuned Nitrogen-Doped Cerium Oxide Exhibits Exceptional Regenerative Free Radical Scavenging Activity in Polymer Electrolytes. *J. Electrochem. Soc.* **2014**, *161*, F1−F9.
(31) Jorge, A. B.; Fraxedas, J.; Cantarero, A.; Williams, A. J.; Rodgers, J.; Attfield, J. P.; Fuertes, A. Nitrogen Doping of Ceria. *Chem. Mater.* **2008**, *20*, 1682−1684.
(32) Wang, Y.; Yin, C.; Qin, H.; Wang, Y.; Li, Y.; Li, X.; Zuo, Y.; Kang, S.; Cui, L. A urea-assisted template method to synthesize mesoporous N-doped CeO_2 for CO_2 capture. *Dalton Trans.* **2015**, *44*, 18718−18722.
(33) Zhang, F.; Wang, P.; Koberstein, J.; Khalid, S.; Chan, S.-W. Cerium oxidation state in ceria nanoparticles studied with X-ray photoelectron spectroscopy and absorption near edge spectroscopy. *Surf. Sci.* **2004**, *563*, 74−82.
(34) Kosacki, I.; Suzuki, T.; Anderson, H. U.; Colomban, P. Raman scattering and lattice defects in nanocrystalline CeO_2 thin films. *Solid State Ionics* **2002**, *149*, 99−105.
(35) Wang, D.; Hui, S.; Liu, C. Mass loss and evolved gas analysis in thermal decomposition of solid urea. *Fuel* **2017**, *207*, 268−273.
(36) Bernhard, A.; Peitz, E.; Wokaun, A.; Kröcher, O. Hydrolysis and thermolysis of urea and its decomposition byproducts biuret, cyanuric acid and melamine over anatase TiO_2. *Appl. Catal., B* **2012**, *115*−*116*, 129−137.
(37) Larson, A. C.; Von Dreele, R. B. General Structure Analysis System (GSAS). In *Los Alamos National Laboratory Report (LAUR)*; 2004; pp 86−748.
(38) Wang, X.; Jiang, Z.; Zheng, B.; Xie, Z.; Zheng, L. Synthesis and shape-dependent catalytic properties of CeO_2 nanocubes and truncated octahedra. *CrystEngComm* **2012**, *14*, 7579−7582.

https://doi.org/10.1021/acsomega.3c01305
ACS Omega 2023, 8, 22646−22655

(39) Gupta, A.; Waghmare, U. V.; Hegde, M. S. Correlation of Oxygen Storage Capacity and Structural Distortion in Transition-Metal-, Noble-Metal-, and Rare-Earth-Ion-Substituted CeO_2 from First Principles Calculation. *Chem. Mater.* **2010**, *22*, 5184−5198.

https://doi.org/10.1021/acsomega.3c01305
ACS Omega 2023, 8, 22646−22655